Unveiling Unprecedented Fine Structure in Coronal Flare Loops with the DKIST

Cole A. Tamburri[1,2,3,5] , Maria D. Kazachenko[1,2,3] , Gianna Cauzzi[1] , Adam F. Kowalski[1,2,3] , Ryan French[2] ,
Rahul Yadav[1,2,3] , Caroline L. Evans[1,3,4] , Yuta Notsu[1,2,3] , Marcel F. Corchado-Albelo[1,2,3] , Kevin P. Reardon[1,3] , and
Alexandra Tritschler[1]

[1] National Solar Observatory, University of Colorado Boulder, 3665 Discovery Drive, Boulder, CO 80303, USA
[2] Laboratory for Atmospheric and Space Physics, University of Colorado Boulder, 3665 Discovery Drive, Boulder, CO 80303, USA
[3] Department of Astrophysical and Planetary Sciences, University of Colorado Boulder, 2000 Colorado Ave, Boulder, CO 80305, USA
[4] Cooperative Institute for Research in Environmental Sciences, 216 UCB Boulder, CO 80309, USA

Abstract

We present the highest-resolution Hα observations of a solar flare to date, collected during the decay phase of an X1.3-class flare on 2024 August 8 at 20:12 UT. Observations with the Visible Broadband Imager at the National Science Foundation's Daniel K. Inouye Solar Telescope (DKIST) reveal dark coronal loop strands at unprecedented spatial resolution in the flare arcade above highly structured chromospheric flare ribbons. After surveying the 20 best-seeing images, we calculate a mean loop width near the top of the arcade of 48.2 km, with a minimum loop width of $\sim$21 km and distribution mode of $\sim$43 km. The distributions of loop widths observed by the DKIST in our study are often symmetric about the mean loop width. This is initial evidence that the DKIST may be capable of resolving the fundamental scale of coronal loops, although further investigation is required to confirm this result. We demonstrate that the resolving power of the DKIST represents a significant step toward advancing modern flare models and our understanding of fine structure in the coronal magnetic field.

Unified Astronomy Thesaurus concepts: Solar flares (1496); Solar corona (1483); Solar coronal loops (1485); Solar active regions (1974); Solar X-ray flares (1816)

Materials only available in the online version of record: animation

1. Introduction

Given our proximity to the Sun, solar flares are the most well-observed high-energy astrophysical phenomena, with a wide range of electromagnetic spectral signatures across the different layers of the solar atmosphere. According to the standard CSHKP flare model (H. Carmichael 1963; P. A. Sturrock 1966; T. Hirayama 1974; R. Kopp & G. Pneuman 1976), reconnection in the solar corona leads to the release of magnetic free energy, precipitation of particles into the chromosphere (e.g., K. Shibata & T. Magara 2011; E. Kontar et al. 2017; A. F. Kowalski 2024), and often, release of a coronal mass ejection (CME) into the heliosphere (e.g., M. D. Kazachenko 2023). Beneath the reconnection site is the posteruption arcade of coronal flare loops (e.g., Z. Švestka 1976; Z. F. Švestka et al. 1987; P. T. Gallagher et al. 2003; M. D. Kazachenko et al. 2022). Following the convention of J. Qiu et al. (2023), we refer to the loops that comprise the arcade as "post-reconnection flare loops" (PRFLs).[6] These PRFLs are filled with hot plasma ($T > 10^7$ K) evaporated from the chromospheric deposition sites and emit at progressively cooler temperatures as the gradual flare decay phase progresses.

Eventually, these loops often emit in Hα during the flare decay phase. From a modeling perspective, the PRFL properties are defined by details of the chromospheric energy deposition, the structure of the three-dimensional magnetic field (G. Aulanier et al. 2012, 2013; M. Janvier et al. 2013; J. T. Dahlin et al. 2016, 2022; J. Qiu et al. 2023; C. A. Tamburri et al. 2024), and the cross-sectional geometry of coronal loops (e.g., J. A. Klimchuk 2001; Z. Mikić et al. 2013; J. A. Klimchuk & C. E. DeForest 2020; J. W. Reep et al. 2022).

Modern hydrodynamic (HD) and radiative-hydrodynamic (RHD) simulations demonstrate the sensitivity of flare and coronal loop evolution to the details of 3D loop geometry. The implications of loop geometry are even important to the evolution of beam-heated flare atmospheres synthesized with the 1D RADYN code (M. Carlsson & R. F. Stein 1992, 1995; J. C. Allred et al. 2005, 2015). For example, a positive gradient in flare loop cross-sectional width along the loop, required to conserve magnetic flux higher in the corona, changes the pitch angle of electrons accelerated into the chromosphere by creating a magnetic mirror within which field-aligned electrons are trapped (A. F. Kowalski 2024). This phenomenon is also relevant to the recently reported delay in signatures of particle precipitation in solar flares (e.g., S. Krucker et al. 2020; B. Chen et al. 2024). Similarly, the Hydrodynamics and Radiation Code (HYDRAD; S. J. Bradshaw & H. E. Mason 2003; J. W. Reep et al. 2013; S. J. Bradshaw & N. M. Viall 2016; J. W. Reep et al. 2018b) has been used in recent years to investigate the cooling times of PRFLs (e.g., J. W. Reep et al. 2020, 2022, 2024). These works demonstrate that loop expansion higher in the corona, variable cross-sectional geometry, and other parameters have a large impact on the draining of loops and spectral signatures associated with the coronal flare response.

---

[5] DKIST Ambassador.

[6] In the past, these have been referred to as "postflare loops" (e.g., H. P. Warren et al. 2018). We use "post-reconnection flare loops" in this work to acknowledge that the flare continues to progress during the observations studied but that the loops are formed as a result of magnetic reconnection associated with the flare.

High-resolution solar observations are crucial to determining input variables for the models described above. Specifically, to constrain loop geometry, it is useful to resolve the smallest coronal "strands" that comprise the arcade. Elementary loops are theorized to have a wide range of cross-sectional widths between 10 and 200 km (e.g., C. Beveridge et al. 2003; H. Peter et al. 2013). These values are smaller than the resolving power of most modern telescopes. Using flare observations from the 1.6 m Goode Solar Telescope at the Big Bear Solar Observatory (BBSO/GST, which has a diffraction limit of $\sim$61 km in Hα), J. Jing et al. (2016) reported very small flare loop widths (ranging from 110 to 161 km). D. Schmidt et al. (2025) performed a similar study with GST data of an off-limb flare arcade and found a median loop width of $\sim$107 km. D. Kuridze et al. (2013) observe loops at a resolution of $\sim$150 km with the Rapid Oscillations in the Solar Atmosphere imager at the Dunn Solar Telescope. The High-resolution Coronal Imager (Hi-C) mission (K. Kobayashi et al. 2014) also reported coronal loop widths of $\sim$200 km (although not associated with a flare), using high-resolution EUV observations (e.g., H. Peter et al. 2013; J. A. Klimchuk & C. E. DeForest 2020). These calculated coronal loop widths are all limited by the resolution of their respective telescopes.

As observations with the Daniel K. Inouye Solar Telescope (DKIST; T. R. Rimmele et al. 2020) 4 m aperture telescope commence, we now have the capability to observe the Sun at unprecedented spatial scales with the Visible Broadband Imager (VBI; F. Wöger et al. 2021). The pixel size of VBI/DKIST Hα images is $0\rlap{.}''017$, half the diffraction limit of DKIST at this wavelength. This provides a resolution at the solar surface of $\sim$24 km, perhaps sufficient to resolve the elementary strands that constitute the arcade of PRFLs.

Here, we present the highest-resolution Hα observations of a solar flare to date, observed with VBI/DKIST during the flare decay phase. We specifically report on fine structure in on-disk PRFLs with structuring on scales roughly 3–4 times smaller than those previously reported with other observing facilities. In Section 2, we describe the DKIST, Solar Dynamics Observatory (SDO), and GOES observations of the X1.3-class flare SOL2024-08-08T19:01:00. In Section 3, we describe our methods for analysis of this data set. In Section 4, we present the results of a statistical study of the widths of 686 PRFLs observed across the 20 best-seeing images. In Section 5, we discuss the implications of this study in the broader context of fine-structure observations and flare modeling. In Section 6, we summarize our main conclusions.

2. Observations

2.1. Summary of the X1.3-class Flare on 2024 August 8: X-Ray Light Curve and Ribbon Structure

A GOES X1.3-class flare occurred in active region NOAA 13777 on 2024 August 8 (start, peak, and end times 19:01 UT, 19:35 UT, and 19:57 UT, respectively; identifier SOL2024-08-08T19:01:00). The flare occurred in two stages. In Figure 1(e), we indicate times of interest in the evolution of this flare, from t_1 to t_5. Prior to t_1, there is a peak in the GOES X-Ray Sensor (GOES/XRS) light curve resulting from a brightening in a different active region. Within the field of view (FOV) eventually covered by DKIST, there is a filament visible in the SDO/Atmospheric Imaging Assembly (AIA) 131 and 304 Å (not shown) at times t_1 and t_2. The first stage (smaller peak in the XRS

1–8 Å light curve between t_1 and t_2) coincides with a smaller reconnection event in loops connecting the region shown in the DKIST images to an eastward region.

During the main reconnection event between t_2 and t_3, the filament mentioned above erupts, likely leading to the CME event listed in the LASCO catalog (N. Gopalswamy et al. 2009, 2024). The peak of the GOES/XRS soft X-ray (SXR) light curve occurs at $\sim$19:35 UT (t_3). The footpoints of the post-reconnection arcade after this eruption are visible as a southern ribbon (S) connecting two sunspots in AR13777 and an upper arc-shaped ribbon (N) in the positive-polarity solar plage (see Figure 1(f) for the Helioseismic and Magnetic Imager (SDO/HMI) magnetogram contextualizing these observations). In this Letter, we investigate detailed observations of flare loops that are present after the CME release, during the decay phase of the flare light curve between t_4 and t_5.

2.2. High-resolution DKIST Observations with the Visible Broadband Imager: Ribbons and PRFLs

The DKIST observations of flare SOL2024-08-08T19:01:00 were collected in fulfillment of experiment ID 2.11. The VBI was observing with the Hα interference filter in the red channel (VBI-red, centered at 656.30 nm with an effective FWHM of $\sim$0.65 Å; DKIST data center product ID L1-ENORQ; $69'' \times 69''$ FOV; Figures 1(a)–(c)) and blue continuum in the blue channel (VBI-blue, centered at 450.3 nm with filter width 4.1 Å; DKIST data center product ID L1-TQFBC; $45'' \times 45''$ FOV; Figure 1(d)). Spatial samplings for VBI-red and VBI-blue images are $0\rlap{.}''017\,\mathrm{pix}^{-1}$ and $0\rlap{.}''011\,\mathrm{pix}^{-1}$, respectively. The raw data have exposure times of 1 ms and 7 ms for the Hα and blue-continuum filters, respectively. The VBI data were speckle reconstructed (F. Wöger et al. 2008), with each reconstructed image (cadence of 2.66 s) produced from 80 raw images. We destretched the image series to further account for atmospheric disturbances but use the speckle-reconstructed, predestretched data during our analysis of PRFL fine structure below. The mean Fried parameter for the data set was $r_0 = 5.4 \pm 2.2$ cm, with a maximum value of $r_0 = 13.0$ cm at 20:55 UT and several periods of successive image frames with $r_0 > 10$ cm (Table 1).

Thin coronal loops connecting ribbons N and S are mostly in absorption in the VBI Hα filter. Each loop is nearly parallel to those in closest proximity, such that there is a clear arcade of coronal loops extending from ribbon N to ribbon S. Around 20:20 UT, strands near the loop top brighten individually as plasma cools through the temperatures to which Hα is sensitive. In each loop, the region of locally brightened plasma begins near the loop top and spreads outward in both directions along the loop, but the loop brightenings are not visible lower in the atmosphere (closer to the ribbons). As the image sequence progresses, loops in the arcade are generally more perpendicular (less sheared) to the two ribbons. Two small sunspots are visible beneath the arcade (clearest in the blue-continuum image, Figure 1(d)).

3. Methods

To determine the cross-sectional widths of dark flare loops observed in the VBI Hα images, we fit a negative-Gaussian empirical model to loops observed in images under the best seeing conditions. A linear function is added to the Gaussian to account for gradients in the intensity of the bright chromospheric backdrop, against which the dark coronal loops are

Table 1
Coronal Loop Width Statistics

Frame	Obs. Time (UT)	r_0 (cm)	Min. Width (km)	Max. Width (km)	Mean Width (km)	δw (km)	Pearson's s	skewtest
(1)	(2)	(3)	(4)	(5)	(6)	(7)	(8)	(9)
0	20:12:32	11.6	25.9	62.5	45.9	3.3	NS	S
1	20:12:35	11.4	23.0	66.4	45.6	3.9	S	S
2	20:12:38	11.5	29.7	59.3	44.4	3.2	NS	S
3	20:12:40	12.2	25.4	83.0	45.1	2.8	NS	NS
4	20:12:43	11.4	28.1	66.4	45.8	3.1	S	S
70	20:15:39	11.0	30.9	90.2	56.3	3.3	S	S
71	20:15:42	11.3	27.8	79.0	49.1	3.4	S	S
174	20:20:16	11.2	25.2	95.3	48.8	3.8	NS	NS
175	20:20:19	10.9	27.0	76.8	47.4	3.6	S	NS
178	20:20:27	11.4	22.8	73.0	44.3	3.6	S	S
261	20:24:08	12.3	27.1	80.4	45.8	3.9	S	NS
262	20:24:11	12.2	21.4	99.7	46.4	4.3	S	NS
263	20:24:13	12.0	28.1	83.4	47.5	3.7	NS	NS
268	20:24:27	10.8	26.3	77.5	49.3	3.5	S	S
269	20:24:30	13.0	25.1	82.2	49.1	3.2	S	S
271	20:24:35	11.0	26.4	107.6	47.5	3.1	NS	NS
272	20:24:37	11.9	25.6	78.3	47.7	4.0	S	S
273	20:24:40	11.6	23.9	94.3	52.3	3.5	S	S
274	20:24:43	11.7	28.3	91.1	52.0	3.9	NS	NS
275	20:24:46	11.8	32.6	84.4	54.4	3.3	S	S

Note. Results from the 20 best-seeing image frames from the 2024 August 8 X1.2-class flare, in order of observation time. In column (1), we indicate the frame number in the VBI data; in column (2), we list the observation time; in column (3), we list the Fried parameter; in columns (4) through (6), we list the minimum, maximum, and mean strand widths, respectively; in column (7), we list the average error in derived strand width; and in columns (8) and (9), we show skewness test results from tests (i) and (ii), where "S" and "NS" indicate that the condition for symmetry was met or was not met, respectively.

visible. The model $L(x)$ is given by the following:

$$L(x) = I_0 e^{\frac{-(x-\mu_x)^2}{2\sigma^2}} + ax + b, \qquad (1)$$

where $L(x)$ is the modeled intensity as a function of position x along an empirically defined profile of the strand; I_0 is the amplitude (negative for the dark loops investigated here); μ_x is the central position of the model; σ is the standard deviation of the model; and a, b are parameters describing the linear fit to the bright background intensity. We use the Python function `scipy.optimize.curve_fit` to perform the fit.

Similarly to the determination of loop widths with the GST reported in J. Jing et al. (2016), we define the width w of each loop to be the FWHM of the fitted Gaussian profile, determined by

$$w = 2\sigma\sqrt{2\ln 2}. \qquad (2)$$

We assume that the loops observed are locally cylindrical, such that projection effects from solar viewing angle do not affect our calculation. As we discuss in Section 5, coronal loops do not necessarily have a circular, nor uniform, cross section. We visually identify each loop and take particular care

to select features that appear as single strands. In a 3D scenario, many strands in the arcade may lie within the same line of sight but at different heights, below the angular separation necessary to resolve the features with VBI Hα. We derive the error in cross-sectional width δw by propagating the error in σ ($\delta\sigma$, an output of the Python fitting function), from which w was determined (Equation (2)):

$$\delta w = |w\sqrt{(\delta\sigma/\sigma)^2}|. \qquad (3)$$

The Fried parameters r_0 associated with the 20 best-seeing images are shown in Table 1. We remove features with calculated error $\delta w > 15$ km in the cross-sectional width from our analysis. This helps to reduce the effects of selection bias by (1) removing features that are likely composed of more than one strand; and (2) removing features that are too faint to reliably determine a width. To verify our results, we perform our analysis several additional times on the five best-seeing image frames. While there are small variations in the calculated widths from these runs, the major results remain the same.

In Figure 2, we show the features selected using image Frame 3 at 20:12:40 UT. We use the same three regions for analysis of each chosen frame. We perform this analysis on the
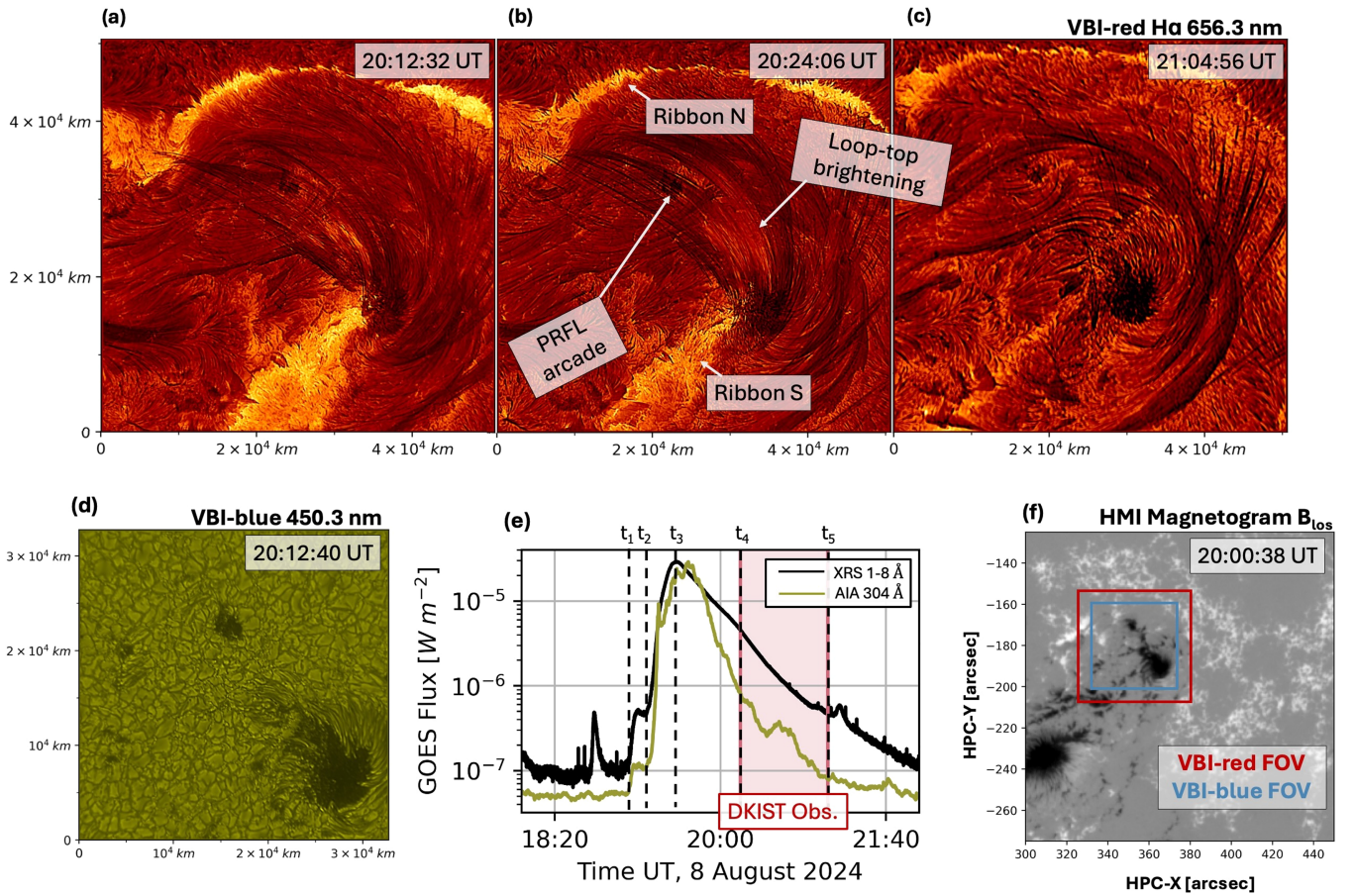
Figure 1. Summary of the GOES/XRS X-ray class X1.3 flare on 2024 August 8. (a)–(c) Images from the VBI-red Hα 656.3 nm filter. In panel (b), we indicate the locations of features discussed in this work, including ribbons N and S, the arcade composed mostly of dark coronal loops, and the loop-top brightening. We include an animation of the speckle-reconstructed, destretched VBI observations of this flare from 20:12 UT to ~20:25 UT, prior to the loss of AO lock. This animation includes the frames shown in panels (a) and (b) here. (d) Image from VBI-blue blue-continuum filter centered at 450.3 nm at the start of DKIST observations. (e) GOES/XRS 1–8 Å SXR and SDO/AIA 304 Å light curves for the event. The shaded region indicates the period of DKIST observations. Dotted vertical lines indicate times of interest in the flare evolution, discussed in Section 2. (f) SDO/HMI line-of-sight magnetogram immediately prior to DKIST observations for context, showing the VBI-red and VBI-blue FOVs in red and blue, respectively.

(An animation of this figure is available in the online article.)

predestretched image sequence in order to avoid the influence of small-scale artifacts of the destretching process.

In Section 4.2, we describe the symmetry of the PRFL width distributions about their mean values. To test the symmetry of a distribution, we use (i) the Pearson median skewness, or second skewness coefficient, defined as $s = 3^*$(mean − median)/(standard deviation), where values of $|s| < 0.5$ indicate reasonable symmetry in the distribution, and (ii) the Python function `scipy.stats.skewtest`, which tests the null hypothesis that the distribution from which a sample is drawn is the same as that of a corresponding normal distribution based on the Fisher–Pearson coefficient of skewness. We note that failure to reject the null hypothesis is not definitive evidence of a symmetric distribution.

4. Results

4.1. Fine Structure of Coronal Loops

In Table 1 we show the results of the Gaussian-fitting width determination analysis for 45 PRFLs in each frame (three selected windows with 15 features per window) in the 20 best-seeing frames (as determined by the Fried parameter) of the speckle-reconstructed VBI data between 20:12 UT and 20:25 UT, the first 13 minutes of observations during which the best

seeing was achieved and adaptive optics (AO) lock was successful. The intensity profiles along the 45 chosen features in Frame 3 (20:12:40 UT), with model fits when appropriate, are shown in Figure 2(e). The mean, minimum, and maximum loop widths are listed in Table 1.

Of the 900 total features investigated across all 20 frames, 214 are poorly fit by the algorithm (indicating that the single-Gaussian fit is not appropriate for these features, most often because of overlapping strands within the line of sight) and are not included in the statistical analysis. Distributions of the cross-sectional widths of the loops observed in the 20 selected frames are shown in Figure 3(a). Figure 3(b) shows the individual calculated cross-sectional widths, with alternating shaded regions corresponding to the first, second, and third regions (from left to right) indicated by red boxes in Figure 2. The minimum calculated PRFL width is 21.4 km, essentially the diffraction limit of the telescope, and the mean widths of the distributions lie between 45 and 55 km. The minimum loop width lies below the ~24 km diffraction limit of DKIST in Hα; this results from our definition of PRFL width (Section 3) and, like in previous works (e.g., D. Schmidt et al. 2025), is likely due to random errors in the Gaussian-fitting process.
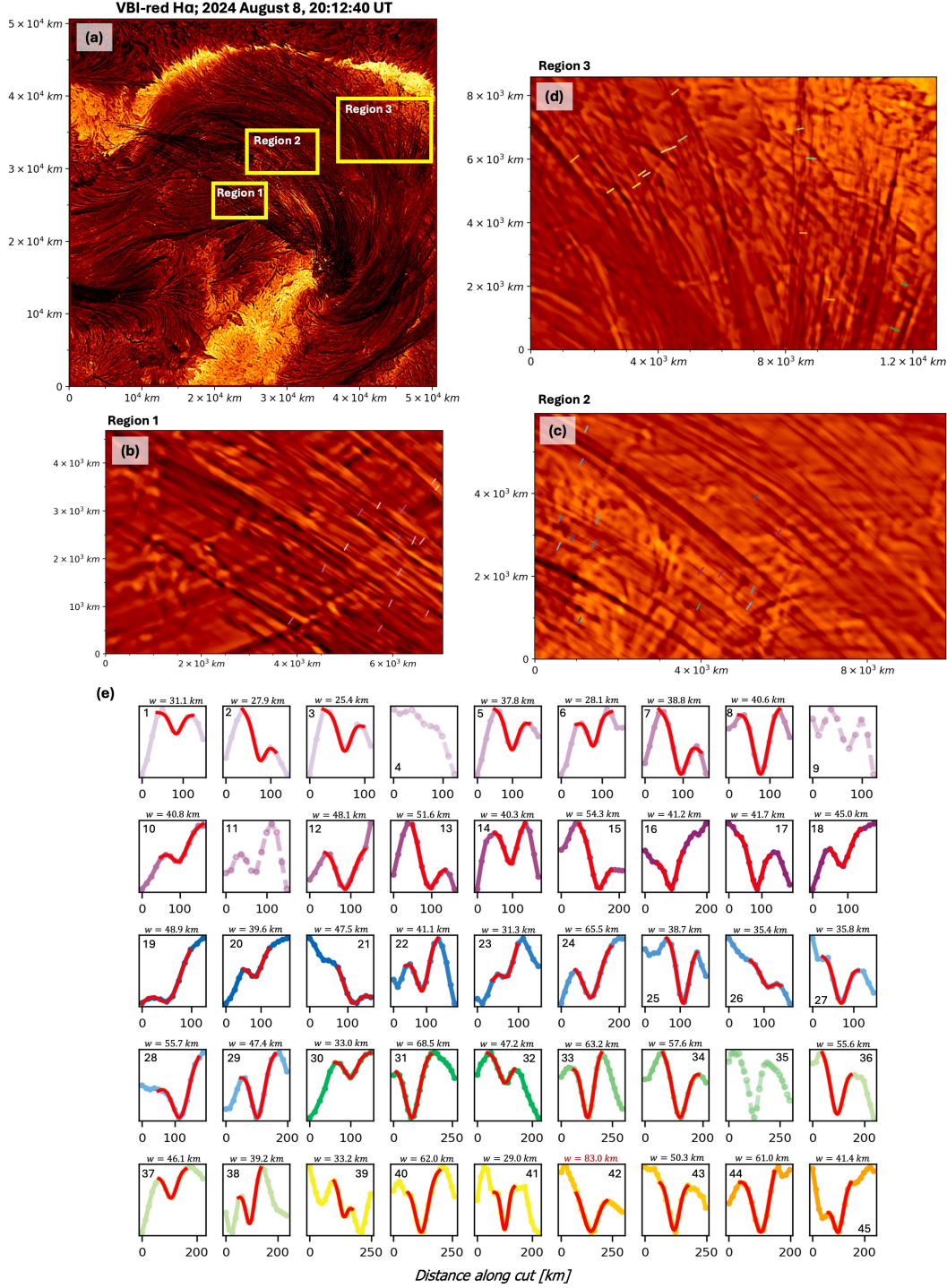
Figure 2. Example of fine-scale coronal strands studied in this work. (a) VBI-red Hα image from 20:12:40 UT ($r_0 = 12.2$ cm). Yellow boxes indicate the three regions near the loop top where we investigate the coronal strand width. (b)–(d) Regions of interest for loop width determination in Section 4.1. Colored line cuts are placed perpendicular to the thin strands investigated here. (e) Intensity profiles along the coronal strands indicated by the cuts in panels (b)–(d). They can vary between ~100 and ~250 km in length. Dots on each profile are separated by ~12 km. Colors indicate the corresponding features in panels (b)–(d). Red solid lines indicate a fit of the data to a function as in Equation (1), from which the FWHM loop width is determined. Dashed intensity profiles without displayed fits in red indicate the features for which the algorithm could not find a successful fit. We note the derived widths of each feature. Axis labels in panels (a)–(d) are in kilometers along the respective axes in the VBI images; in panel (e), axis labels are in kilometers along the perpendicular cuts.

4.2. Symmetry about the Mean of PRFL Width Distributions

E. Scullion et al. (2014) discuss that a representative sample of the true physical distribution of cross-sectional PRFL widths should be Gaussian or otherwise symmetric around the peak "typical" strand width. However, distributions of these widths from other observatories have often shown an exponential increase in the number of features at the finest scales resolvable by those instruments (e.g., E. Scullion et al. 2014). For higher-resolution observations, for example with the GST, distributions are more peaked with tails at larger and
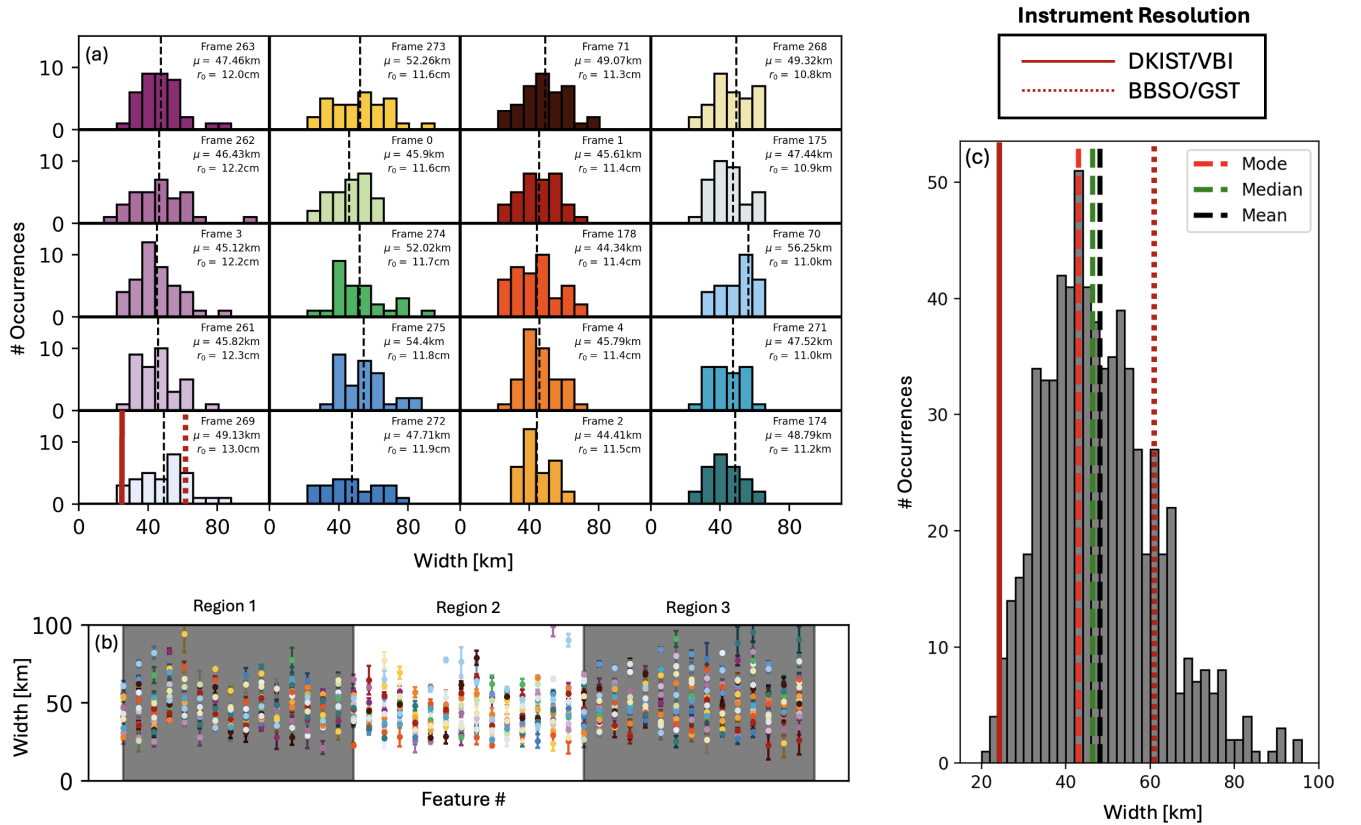
Figure 3. Summary of loop widths in each of the 20 best-seeing image frames indicated in Table 1. (a) Histograms of the loop width distributions in each frame. Colors do not correspond to those in Figure 2(e). Black dotted vertical lines indicate the distribution means. The third panel in the leftmost column is the distribution corresponding to the features shown in Figure 2. Vertical red lines in the bottom panel of the leftmost column indicate the spatial resolution of DKIST/VBI and BBSO/GST. (b) Loop widths with errors for all frames studied. Alternating shaded regions indicate the features from each of the three regions in Figure 2, which are the same for all 20 frames. (c) Combined distribution of calculated widths from all 20 frames, with the mean and median of the distribution and the VBI and GST resolution limits indicated.

smaller scales, although still with a longer tail at larger loop widths (J. Jing et al. 2016; D. Schmidt et al. 2025). The asymmetry indicates that we have until now been unable to produce a distribution of strand cross-sectional widths reflecting the fundamental loop widths. In this data set, the distributions of loop widths from individual frames (Figure 3(a)) are often symmetric. Figure 3(c) shows the distribution of loop widths across all 20 frames, with median 46 km and mean 48 km. The results of tests of symmetry (i) and (ii) for each distribution are listed in the last two columns of Table 1. Thirteen of 20 and 12 of 20 distributions pass the first and second tests of symmetry, respectively. The distribution of all widths in Figure 3(c) passes the first test of symmetry ($s \approx 0.4$) but not the second. As a caveat, some distributions that do not pass one or both tests (e.g., corresponding to Frame 3 (Figure 2) and the combined distribution in Figure 3(c)) are penalized significantly for a few strands with widths ~75% greater than the mean width of the distribution. The strands with large calculated widths may in reality be structures composed of many strands within the same line of sight (e.g., strand number 42 in the case of Frame 3, with width highlighted in red in Figure 2(e)). Removal of these specific structures from the samples changes the result of the tests to favor symmetry, possibly including the combined distribution (i.e., our determination of whether a distribution can be considered symmetric is conservative).

5. Discussion

The ~20–80 km widths of resolved coronal magnetic structures reported in this study have major implications in our understanding of coronal evolution during a flare. For example, the mechanism by which the cross section of a loop expands with height into the corona (due to the decrease of magnetic pressure with height and the requisite conservation of magnetic flux) is physically justified, but the expansion of coronal loops has never been clearly observed (e.g., J. A. Klimchuk 2001; J. A. Klimchuk & C. E. DeForest 2020; J. W. Reep et al. 2022). In the absence of decisive observations, this fundamental assumption has been challenged. In an observational study, J. A. Klimchuk (2001) suggested that the cross-sectional widths of coronal loops do not vary along their length, while H. Peter & S. Bingert (2012) argue that the interpretation of this analysis may be more complicated. Due to the response functions of observed lines, only a narrow portion of the imaged coronal loop might be within the range of temperatures and densities to which any specific line is sensitive, giving the impression of a loop of constant width from photosphere to corona. Z. Mikić et al. (2013) note that cross-sectional expansion should be an assumed property of loop models, rather than an optional parameter, and demonstrate that processes such as coronal rain require geometrical nonuniformity.

Besides the loop expansion, the shape and eccentricity of the loop cross section introduce another set of important

parameters for both PRFLs and loops not associated with a flare (e.g., S. K. Antiochos & P. A. Sturrock 1976; C. J. Schrijver et al. 1989; J. A. Klimchuk 2001; A. A. van Ballegooijen et al. 2011; J. A. Klimchuk & C. E. DeForest 2020 and references therein), although there may be relevant physical differences between flare-related and nonflare loop geometry. J. A. Klimchuk & C. E. DeForest (2020) use Hi-C observations of 20 coronal loops to argue that observed flux tubes are approximately circular but that the unresolved loops may be composed of many strands of nonuniform cross section. Our observations align with this concept: the flare loops measured in our work are more than an order of magnitude smaller than the loops resolvable in Hi-C observations, suggesting that large, underresolved, measurably circular structures in past works could potentially be composed of many smaller $\sim$20–80 km wide loops. Even the largest loop observed by the DKIST in this study is smaller than the vast majority of loops recorded by BBSO/GST, the telescope with the next-best resolving power (e.g., J. Jing et al. 2016; D. Schmidt et al. 2025). A future study could investigate flare loops observed by both instruments simultaneously and test whether the larger structures measured by previous works are composed of smaller loops resolvable by the DKIST.

Properly constrained loop width is also relevant when considering the processes associated with flare heating, both in the corona and lower atmosphere. For example, J. Qiu & D. W. Longcope (2016) explain the long duration of gradual flare heating in SDO/AIA observations channels by assuming that each loop observed by SDO is composed of many individually heated strands, although the number of strands is undetermined. M. Litwicka et al. (2025) use the FLARIX code to address the remaining discrepancy between the modeled and observed intensities of chromospheric lines by assuming flare heating is provided by short pulses in unresolved filament structures. J. W. Reep et al. (2018a) use HYDRAD to investigate the impact of multithreaded heating on synthetic Si IV and Fe XXI lines, assuming a uniform loop cross section. However, these works necessarily assume or infer coronal filling factors and relative loop widths. The resolving power of the DKIST provides a valuable constraint on the loop width parameter, which may significantly improve such models. Additionally, the relevance of spatially resolved flare loops and implications in flare heating go beyond the Sun; even in the case of stellar flares, heating of coronal loops associated with a flare has recently garnered attention as a potential mechanism for observed late-phase emission (e.g., P. Heinzel & K. Shibata 2018; K. E. Yang et al. 2023; T. Otsu et al. 2024).

Beyond the typical strand size, accurately constrained loop geometry is relevant to modeling the hydrodynamics (and even radiative hydrodynamics) of a flare (e.g., Z. Mikić et al. 2013; J. W. Reep et al. 2022; J. W. Reep & V. S. Airapetian 2023; A. F. Kowalski 2024; J. W. Reep et al. 2024), as discussed in Section 1. Even without the aid of these loop models, A. G. Emslie & L. K. Wilkinson (1994) performed an early study investigating the asymmetry of flux tubes. Without sufficient resolving power, it is impossible to observationally determine the relevant parameters (such as cross-sectional area and eccentricity) to validate these experiments. DKIST also provides the opportunity for a new multifilter investigation of observed loops beyond just Hα (e.g., in Ca II K) in order to constrain PRFL geometry in comparison to modern loop

models. Even if the temperature response function of an individual filter prohibits single-line determination of the relevant geometrical properties (as suggested by H. Peter & S. Bingert 2012), simultaneous observation of elementary structures with many filters could place additional constraints on hydrodynamical models, potentially presenting a solution to the problem at unprecedented scales.

Even with the high resolution of DKIST/VBI, it is unclear whether the actual characteristic loop widths might be even smaller than the diffraction limit of the DKIST. The symmetry argument in Section 4.2, which demonstrates that a distribution of loop widths measured with the VBI under ideal seeing conditions is often centered around the typical loop width, presents evidence that the DKIST is capable of resolving most elementary Hα loops. We note that the distribution of loop widths produced by D. Schmidt et al. (2025) using higher-resolution GST observations is right skewed but is still more symmetric than distributions produced using lower-resolution observations (e.g., by the Swedish Solar Telescope as in E. Scullion et al. 2014). We note that the GST observations were taken of off-limb loops rather than the dark on-disk structures we study, and so the two may not be directly analogous. However, the similarity between the two produced distributions presents the possibility that the typical loop widths observed with VBI may still lie above a characteristic width, albeit at a higher resolution than GST. To test the possibility that DKIST can observe most fundamental PRFLs more rigorously, the spectral and thermodynamic properties of the observed strands could be compared to realistic simulations like HYDRAD (e.g., spectral line intensity and loop cooling time, as in J. W. Reep et al. 2022). Although these models are 1D, the magnetic field strength and other properties can be varied in these models to reflect the practical impacts of geometrical variation. If the evolution of the modeled and observed loops are relatively in agreement, this would provide further evidence to support our result. Comparison to future 3D models or mathematical predictions of expected loop width (e.g., H. Peter et al. 2013) could also be employed.

We note also that smaller coronal loop widths than we observe here have been estimated from mathematical arguments in the past. Studying the same flare as J. A. Klimchuk & C. E. DeForest (2020), H. Peter et al. (2013) estimate that coronal loops observed near the chromosphere may be composed of strands with widths far smaller ($\sim$15 km) than the $\sim$45 km cross-sectional loop width that we claim using the VBI data. They use 193 Å images with the Hi-C rocket for their analysis and note that loop cross sections will vary based on the wavelength of observations and the filling factor of bright coronal plasma. The maximum estimated width in Hα may therefore differ. We also note that the loops studied by H. Peter et al. (2013), while observed in an active region, were not associated with a flare. The high temperatures associated with coronal flare loops could also potentially impact the predicted loop widths. Additionally, their analysis does not address the important effects of loop expansion or noncircular cross section. Other studies (e.g., D. H. Brooks et al. 2012) estimate larger strand widths, indicating that the question of fundamental strand width can only be directly resolved through observations.

The data studied by J. Jing et al. (2016) were taken using a Fabry–Perot-based, 0.07 Å FWHM filter centered at Hα + 1.0 Å, while the DKIST observations discussed here

are taken at line center with a filter width of ∼0.65 Å. This detail may account for some difference in the measured loop widths with these respective telescopes, although a precise investigation of this impact will require an analysis of full spectral profiles or the derivation of temperatures and densities from loop modeling, coupled with a full 3D radiative transfer treatment of Hα (e.g., J. Leenaarts et al. 2012; J. P. Bjørgen et al. 2019). We note that the loops are dark in the Hα images from both telescopes, indicating there is a net absorption in both passbands, which would be due to a combination of a changed temperature, density, populations, and velocity of the plasma in these loops. The broader VBI filter shows more contributions from the photospheric layers in the wings of the profile, resulting in some faint granulation visible in Figures 1(a)–(c). Since the identification of coronal loops relies upon the contrast with respect to other nearby emission, the enhanced photospheric background with an interference filter may make it more difficult to identify PRFLs with DKIST when compared to GST. However, since the loops observed with the two filters are at least morphologically similar, and both resolve down to the diffraction limit of their respective telescopes, the most likely explanation for the differences in measured loop width is that the PRFLs observed by DKIST are simply unresolved by GST.

Whether or not the DKIST is capable of observing a large number of elementary coronal loops, the flare observations here have highlighted complications in the pursuit of observationally characterizing loop shape and evolution, including seeing, temperature sensitivity of the observed line, and projection effects. Many of the coronal loops observed in our data are only visible in Hα for a portion of their extent, possibly supporting the notion that temperature variations along a loop have a significant impact on our ability to investigate coronal loop geometry—but we note that the Hα strength in these loops may be sensitive to many other physical parameters. It is also possible that the distributions of loop widths shown in Figure 3, while more often symmetric than those presented in previous works, may still be somewhat limited by the resolution of the DKIST at the finest scales. To validate and expand these results, the analysis should be performed for more events and for other spectral passbands.

6. Conclusions

The geometry of coronal loops has significant implications in many aspects of solar physics, including detailed modeling of PRFL thermal evolution and coronal structure in the absence of a flare. However, the widths of elementary loops, theorized at ∼10–200 km, have historically been below the resolution limits of modern telescopes. The 4 m DKIST has the capability to observe structures less than half the size of the smallest-observable features in the past and could possibly resolve a significant portion of elementary coronal loops.

We use DKIST/VBI Hα observations of the decay phase of the X1.3-class flare SOL2024-08-08T19:01:00 to analyze fine structure of PRFL strands and compare these with previous observations. Our major findings are as follows:

1. We find that DKIST observations reveal fine structure at or near the diffraction limit of the DKIST in the flare loops and flare ribbons. Observations of this flare at such high resolution and cadence are the first of their kind and provide fertile ground for future investigations of the solar flare dynamics.
2. We measure the widths of 686 PRFLs across the 20 best-seeing frames and find average loop widths of 44 km < w < 56 km, with minimum loop widths at the diffraction limit (∼24 km in Hα). On average, these strands are ∼45% smaller than the next-smallest observed Hα PRFLs captured by the GST at BBSO (J. Jing et al. 2016).
3. According to two tests of the symmetry of loop width distributions, we find that 13 out of 20 and 12 out of 20 of the distributions pass tests of symmetry with statistical significance. The symmetry of loop distributions provides preliminary evidence that the DKIST/VBI can resolve most elementary flare loops.
4. From the discovered symmetrical loop width distributions, we conclude that previous studies of coronal loop geometry have been limited by insufficient telescope resolution. This result suggests that the DKIST data could provide valuable constraints on modern HD and RHD flare models.

This is the first high-resolution solar flare study with DKIST/VBI in Hα. The resolution achieved by the DKIST demonstrates significant substructures well below the scales previously observable, indicating that it is now both possible and necessary to revisit past models of arcade structure in the context of high-resolution DKIST observation. Since both the dark loops in the posteruption arcade and bright flare ribbons are visible in Hα, a future study may investigate the common spatial scales between these two regions, testing the connectivity between sites of chromospheric energy deposition and the coronal loop structures resulting from magnetic reconnection. We anticipate that these observations will represent the first of many from the DKIST to be used to investigate the role of fine structure in flare heating, placing additional constraints on modern simulations and contributing to a detailed picture of flare evolution in the chromosphere and corona.

ORCID iDs

Cole A. Tamburri ⓘ https://orcid.org/0000-0002-3229-1848
Maria D. Kazachenko ⓘ https://orcid.org/0000-0001-8975-7605

Gianna Cauzzi ⓘ https://orcid.org/0000-0002-6116-7301
Adam F. Kowalski ⓘ https://orcid.org/0000-0001-7458-1176
Ryan French ⓘ https://orcid.org/0000-0001-9726-0738
Rahul Yadav ⓘ https://orcid.org/0000-0003-4065-0078
Caroline L. Evans ⓘ https://orcid.org/0000-0002-6478-3281
Yuta Notsu ⓘ https://orcid.org/0000-0002-0412-0849
Marcel F. Corchado-Albelo ⓘ https://orcid.org/0000-0003-1597-0184
Kevin P. Reardon ⓘ https://orcid.org/0000-0001-8016-0001
Alexandra Tritschler ⓘ https://orcid.org/0000-0003-3147-8026

References

Allred, J. C., Hawley, S. L., Abbett, W. P., & Carlsson, M. 2005, ApJ, 630, 573
Allred, J. C., Kowalski, A. F., & Carlsson, M. 2015, ApJ, 809, 104
Antiochos, S. K., & Sturrock, P. A. 1976, SoPh, 49, 359
Aulanier, G., Démoulin, P., Schrijver, C. J., et al. 2013, A&A, 549, A66
Aulanier, G., Janvier, M., & Schmieder, B. 2012, A&A, 543, A110
Beveridge, C., Longcope, D. W., & Priest, E. R. 2003, SoPh, 216, 27
Bjørgen, J. P., Leenaarts, J., Rempel, M., et al. 2019, A&A, 631, A33
Bradshaw, S. J., & Mason, H. E. 2003, A&A, 401, 699
Bradshaw, S. J., & Viall, N. M. 2016, ApJ, 821, 63
Brooks, D. H., Warren, H. P., & Ugarte-Urra, I. 2012, ApJ, 755, L33
Carlsson, M., & Stein, R. F. 1992, ApJ, 397, L59
Carlsson, M., & Stein, R. F. 1995, ApJ, 440, L29
Carmichael, H. 1964, in Proceedings of the AAS-NASA Symposium, ed. Wilmot Hess (Washington, D.C.: NAASP), 451
Chen, B., Kong, X., Yu, S., et al. 2024, ApJ, 971, 85
Dahlin, J. T., Antiochos, S. K., Qiu, J., & Devore, C. R. 2022, ApJ, 932, 94
Dahlin, J. T., Drake, J. F., & Swisdak, M. 2016, PhPl, 23, 120704
Emslie, A. G., & Wilkinson, L. K. 1994, ApJ, 431, 873
Gallagher, P. T., Dennis, B. R., Krucker, S., Schwartz, R. A., & Tolbert, A. K. 2003, in The Reuven Ramaty High-Energy Solar Spectroscopic Imager (RHESSI), ed. R. P. Lin, B. R. Dennis, & A. O. Benz (Dordrecht: Springer), 341
Gopalswamy, N., Michałek, G., Yashiro, S., & Manchester, W. 2024, arXiv:2407.04165
Gopalswamy, N., Yashiro, S., Michalek, G., et al. 2009, EM&P, 104, 295
Heinzel, P., & Shibata, K. 2018, ApJ, 859, 143
Hirayama, T. 1974, SoPh, 34, 323
Janvier, M., Aulanier, G., Pariat, E., & Démoulin, P. 2013, A&A, 555, A77
Jing, J., Xu, Y., Cao, W., et al. 2016, NatSR, 6, 24319
Kazachenko, M. D. 2023, ApJ, 958, 104

Kazachenko, M. D., Albelo-Corchado, M. F., Tamburri, C. A., & Welsch, B. T. 2022, SoPh, 297, 59
Klimchuk, J. A. 2001, in Physics of the Solar Corona and Transition Region, ed. O. Engvold & J. W. Harvey (Dordrecht: Springer), 53
Klimchuk, J. A., & DeForest, C. E. 2020, ApJ, 900, 167
Kobayashi, K., Cirtain, J., Winebarger, A. R., et al. 2014, SoPh, 289, 4393
Kontar, E., Perez, J., Harra, L., et al. 2017, PhRvL, 118, 155101
Kopp, R., & Pneuman, G. 1976, SoPh, 50, 85
Kowalski, A. F. 2024, LRSP, 21, 1
Krucker, S., Masuda, S., & White, S. M. 2020, ApJ, 894, 158
Kuridze, D., Mathioudakis, M., F Kowalski, A., et al. 2013, A&A, 552, A55
Leenaarts, J., Carlsson, M., & Rouppe van der Voort, L. 2012, ApJ, 749, 136
Litwicka, M., Heinzel, P., & Kašparová, J. 2025, ApJ, 983, 155
Mikić, Z., Lionello, R., Mok, Y., Linker, J. A., & Winebarger, A. R. 2013, ApJ, 773, 94
Otsu, T., Asai, A., Ikuta, K., & Shibata, K. 2024, ApJL, 974, L13
Peter, H., & Bingert, S. 2012, A&A, 548, A1
Peter, H., Bingert, S., Klimchuk, J. A., et al. 2013, A&A, 556, A104
Qiu, J., Alaoui, M., Antiochos, S. K., et al. 2023, ApJ, 955, 34
Qiu, J., & Longcope, D. W. 2016, ApJ, 820, 14
Reep, J. W., & Airapetian, V. S. 2023, ApJ, 958, 9
Reep, J. W., Antolin, P., & Bradshaw, S. J. 2020, ApJ, 890, 100
Reep, J. W., Bradshaw, S. J., & McAteer, R. T. 2013, ApJ, 778, 76
Reep, J. W., Polito, V., Warren, H. P., & Crump, N. A. 2018a, ApJ, 856, 149
Reep, J. W., Russell, A. J., Tarr, L. A., & Leake, J. E. 2018b, ApJ, 853, 101
Reep, J. W., Scott, R. B., Chhabra, S., Unverferth, J., & Knizhnik, K. J. 2024, ApJ, 967, 53
Reep, J. W., Ugarte-Urra, I., Warren, H. P., & Barnes, W. T. 2022, ApJ, 933, 106
Rimmele, T. R., Warner, M., Keil, S. L., et al. 2020, SoPh, 295, 172
Schmidt, D., Schad, T. A., Yurchyshyn, V., et al. 2025, NatAs, in press
Schrijver, C. J., Lemen, J. R., & Mewe, R. 1989, ApJ, 341, 484
Scullion, E., van der Voort, L. R., Wedemeyer, S., & Antolin, P. 2014, ApJ, 797, 36
Shibata, K., & Magara, T. 2011, LRSP, 8, 6
Sturrock, P. A. 1966, Natur, 211, 695
Švestka, Z. 1976, Geophysics and Astrophysics Monographs (Dordrecht: Reidel)
Švestka, Z. F., Fontenla, J. M., Machado, M. E., et al. 1987, SoPh, 108, 237
Tamburri, C. A., Kazachenko, M. D., & Kowalski, A. F. 2024, ApJ, 966, 94
van Ballegooijen, A. A., Asgari-Targhi, M., Cranmer, S. R., & DeLuca, E. E. 2011, ApJ, 736, 3
Warren, H. P., Brooks, D. H., Ugarte-Urra, I., et al. 2018, ApJ, 854, 122
Wöger, F., Rimmele, T., Ferayorni, A., et al. 2021, SoPh, 296, 145
Wöger, F., von der Lühe, O., & Reardon, K. 2008, A&A, 488, 375
Yang, K. E., Sun, X., Kerr, G. S., & Hudson, H. S. 2023, ApJ, 959, 54